CHEMISTRY OF MATERIALS

pubs.acs.org/cm

Article

Synthesis and Stability Phase Diagram of Topological Semimetal Family $LnSb_xTe_{2-x-\delta}$

Published as part of Chemistry of Materials special issue "In Memory of Prof. Francis DiSalvo".

Tyger H. Salters, James Colagiuri, Andre Koch Liston, Josh Leeman, Tanya Berry, and Leslie M. Schoop*

Cite This: https://doi.org/10.1021/acs.chemmater.4c02198

Read Online

ACCESS | Metrics & More | Article Recommendations | Supporting Information

ABSTRACT: The solid solution $LnSb_xTe_{2-x-\delta}$ (Ln = lanthanide) is a family of square-net topological semimetals that exhibit tunable charge density wave (CDW) distortions and band filling dependent on x, offering broad opportunities to examine the interplay of topological electronic states, CDW, and magnetism. While several Ln series have been characterized, gaps in the literature remain, inviting a systematic survey of the remaining composition space that is synthetically accessible. We present our efforts to synthesize $LnSb_xTe_{2-x-\delta}$ across the remaining lanthanides via chemical vapor transport. Compiling our results with the reported literature, we generate a stability phase diagram across the ranges of Ln and x. We find a stability boundary for intermediate x beyond Tb, while x = 1 and x = 0 can be isolated up to Ho and Dy, respectively. SEM and XRD analyses of unsuccessful reactions indicated the formation of several stable binary phases. The presence of structurally related $LnTe_3$ in samples suggests that stability is limited by the size of Ln, due to increasing compressive strain along the layer stacking axis with decreasing size. Finally, we demonstrate that late Ln can be stabilized in $LnSb_xTe_{2-x-\delta}$ via substitution into larger Ln members, synthesizing $La_{1-y}Ho_ySb_xTe_{2-x-\delta}$ as a proof of concept.

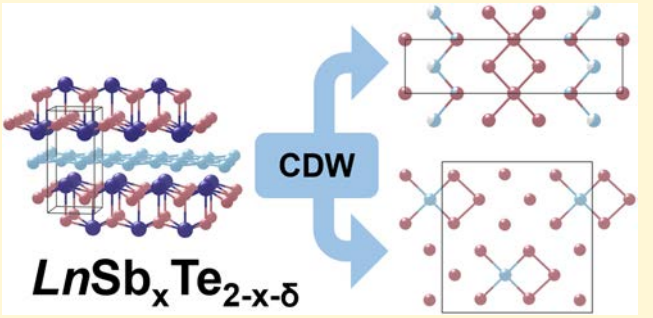

INTRODUCTION

As the field of topological quantum materials approaches maturity, square-net materials, named for their shared structural motif, have been established as frequent hosts to topological electronic states.[1−8] The arrangement of half-filled p_x and p_y orbitals on the square-net sublattice yields multiple topologically protected band crossings near the Fermi energy E_F, resulting in a family of Dirac, Weyl, and nodal line topological semimetals (TSMs), and topological insulators.[9−12] The square net is stabilized by delocalized, hypervalent bonding, where the degenerate p_x/p_y band is exactly half-filled when an ideal electron count of $6e^-$/atom is fulfilled, placing E_F at the nodal line protected by m_z mirror symmetry.[13] This electron delocalization results in metallic conductivity and high electron mobility due to the sharply dispersed bands. The bonding of the square net also affords Dirac nodes protected by nonsymmorphic n glide symmetry, present at band fillings above (and below) the ideal electron count. Hypervalent bonding becomes unstable at this higher band filling, which is resolved by forming a charge density wave (CDW), where bond localization results in a periodic structural distortion breaking the degeneracy of the p_x/p_y band (analogous to Jahn−Teller distortion that stabilizes a half-filled degenerate state in a single molecule).[14] The periodicity of the CDW distortion is described by propagation wavevector $\mathbf{q}$ in reciprocal space, corresponding to the commensurate or incommensurate expansion of the unit cell required to represent the structural modulation.[15]

$LnSb_xTe_{2-x-\delta}$ (Ln = lanthanide, δ = vacancy concentration) is a family of square-net derived Zintl-phase materials, where the 1:1:1 stoichiometric end members are isostructural to canonical nodal line semimetal ZrSiS,[11] where the polyanionic Sb^- square net is sandwiched between distorted rock-salt $Ln^{3+}Te^{2-}$ layers. The solid solution permits the substitution of Te into the Sb net, resulting in a chemically tunable platform to control band filling, where E_F can be shifted to access the nonsymmorphic Dirac crossing. This materials design strategy is set apart from the work done to predict new topological materials using computational databases, as solid solutions are not typically addressed due to the limits of the computationally inexpensive methods used to calculate tentative band structures.[16−19] Several of the end members, LnSbTe and

Received: August 5, 2024
Revised: November 19, 2024
Accepted: November 20, 2024

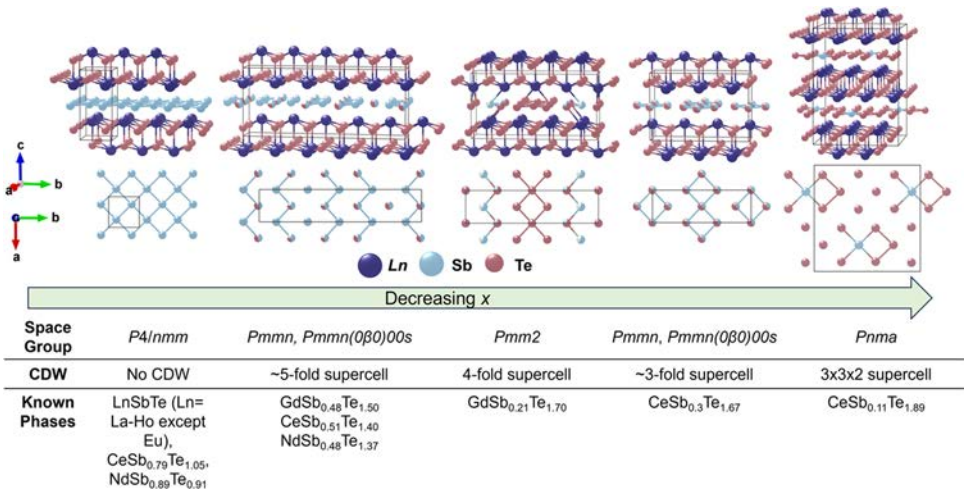

Space Group	P4/nmm	Pmmn, Pmmn(0β0)00s	Pmm2	Pmmn, Pmmn(0β0)00s	Pnma
CDW	No CDW	~5-fold supercell	4-fold supercell	~3-fold supercell	3x3x2 supercell
Known Phases	LnSbTe (Ln= La-Ho except Eu), $CeSb_{0.79}Te_{1.05}$, $NdSb_{0.89}Te_{0.91}$	$GdSb_{0.48}Te_{1.50}$ $CeSb_{0.51}Te_{1.40}$ $NdSb_{0.48}Te_{1.37}$	$GdSb_{0.21}Te_{1.70}$	$CeSb_{0.3}Te_{1.67}$	$CeSb_{0.11}Te_{1.89}$

Figure 1. Evolution of structure and CDW in $LnSb_xTe_{2-x-\delta}$. As x decreases, the delocalized bonding of the Sb square net is broken, resulting in a variety of commensurately and incommensurably modulated superstructures. As the CDW evolves, the Sb/Te atoms in the distorted net localize into assorted bonding motifs, such as chains, fused four-membered rings, and functionalized four-membered rings. Crystal structures and reported compounds are reproduced in the literature.[39,40,43]

$LnTe_2$, were synthesized and studied long before their rediscovery as TSM candidates.[20−22] Several LnSbTe have been identified as nodal line semimetal candidates by theoretical calculations, with many confirmed as TSMs using angle-resolved photoelectron spectroscopy (ARPES).[23−31] Structural distortions due to CDWs have been well documented across $LnTe_2$, where the prevalence of vacancy in the Te square net provides some initial insight into the electronic instability of the square net with high e^- counts.[21,32−36] In charge-balancing stoichiometric $LnTe_2$, the $Ln^{3+}Te^{2-}$ layer necessitates a net −1 charge across the square net, yielding an unstable $7e^-$/Te atom. The CDW distortion of the square net increases the covalent character of bonding in the layer, as it breaks down into a variety of smaller polyanionic units, where vacancy accounts for any remaining charge balance.

For all previously studied Ln (with the exception of Sm[37]), the tetragonal parent structure (isostructural to ZrSiS) is stable to some critical x, unique to each Ln, after which $LnSb_xTe_{2-x-\delta}$ exhibits a continuously evolving CDW with a rich structural phase diagram, summarized in Figure 1. At intermediate **x**, the tetragonal symmetry of the square net breaks into an orthorhombic CDW phase described by a single, unidirectional propagation wavevector pointing along the longer in-plane axis b.[38−40] The periodicity of the CDW decreases with increasing x, as bond localization breaks the net into zigzag chains, and then into fused four-member rings. Notably, at the 4-fold CDW point, both of these structural moieties coexist in a structure with space group *Pmm*2, indicating loss of glide plane symmetry which is then re-entrant with increasing x.[39] Distortions become increasingly complex at $x < 0.2$, where the CDW must be described using multiple **q**, as stacking order expands the unit cell in all crystallographic directions coinciding with further electronic localization, yielding a square net that has distorted into functionalized four-member rings with isolated atoms, as in $CeSb_{0.11}Te_{1.89}$.[40] Beyond their intricate structural chemistry, unique electronic properties have been linked to the presence of CDWs in $LnSb_xTe_{2-x-\delta}$. While the formation of a CDW is typically associated with the opening of a band gap at E_F, ARPES has confirmed the presence of Dirac points in $GdSb_{0.48}Te_{1.46}$ and $CeSb_{0.11}Te_{1.89}$.[41,42] Furthermore, in both phases, topologically trivial bands were found to have been selectively gapped away from E_F, indicating that the CDW can be used as a tool to "clean" trivial bands.

The presence of magnetic rare-earth ions in $LnSb_xTe_{2-x-\delta}$ also presents a myriad of opportunities to investigate the interplay of topological states with magnetism, with the potential to discover new quantum phenomena. Many of the LnSbTe phases are antiferromagnetic at low temperatures, exhibiting either collinear or complex magnetic structures determined by neutron diffraction.[24−27,29−31,43−48] Under applied magnetic field, CeSbTe can be switched between Dirac and Weyl states,[24] which suggests an interaction between Ln^{3+} spins and electronic states derived from the Sb square net. This likely occurs via the Ruderman−Kittel−Kasuya−Yosida (RKKY) interaction, where conduction electrons mediate the spin exchange. RKKY interaction also likely drives complex magnetism in CDW phases; several Ln display rich magnetic phase diagrams with multiple field- or temperature-induced transitions that evolve with x, indicative of the potential for $LnSb_xTe_{2-x-\delta}$ to host to a variety of unique magnetic and quantum phenomena.[37,40,43,49,50] For example, "devil's staircase" behavior and colossal magnetoresistance are observed in $CeSb_{0.11}Te_{1.89}$.[42] Enhanced magnetic entropy in $GdSb_{0.46}Te_{1.48}$ suggests that compositional tuning of RKKY interaction might also afford skyrmion phases in $LnSb_xTe_{2-x-\delta}$.[49] Our recent neutron diffraction studies of $NdSb_xTe_{2-x-\delta}$ provide the most direct observation of magnetic coupling to CDW, where we find an integer relationship between the propagation wavevectors of the CDW and elliptical cycloid magnetic structure such that the CDW "templates" the spin modulation.[43]

While $LnSb_xTe_{2-x-\delta}$ already hosts a wide variety of interesting physics, the full range of synthetically accessible compounds remains unknown. Herein, we present our efforts to fill in the remaining synthetic gaps in the $LnSb_xTe_{2-x-\delta}$ family, yielding a stability phase diagram across all Ln atoms for $0 \leq x \leq 1$. While synthesis of $x = 1$ phase is possible up to DySbTe, $x < 1$ phases could not be obtained for Ln smaller than Tb. The stability of these nonstoichiometric phases resembles that of their corresponding $x = 0$ phases, where the decreasing size of Ln decreases lattice stability. We then

https://doi.org/10.1021/acs.chemmater.4c02198
Chem. Mater. XXXX, XXX, XXX−XXX

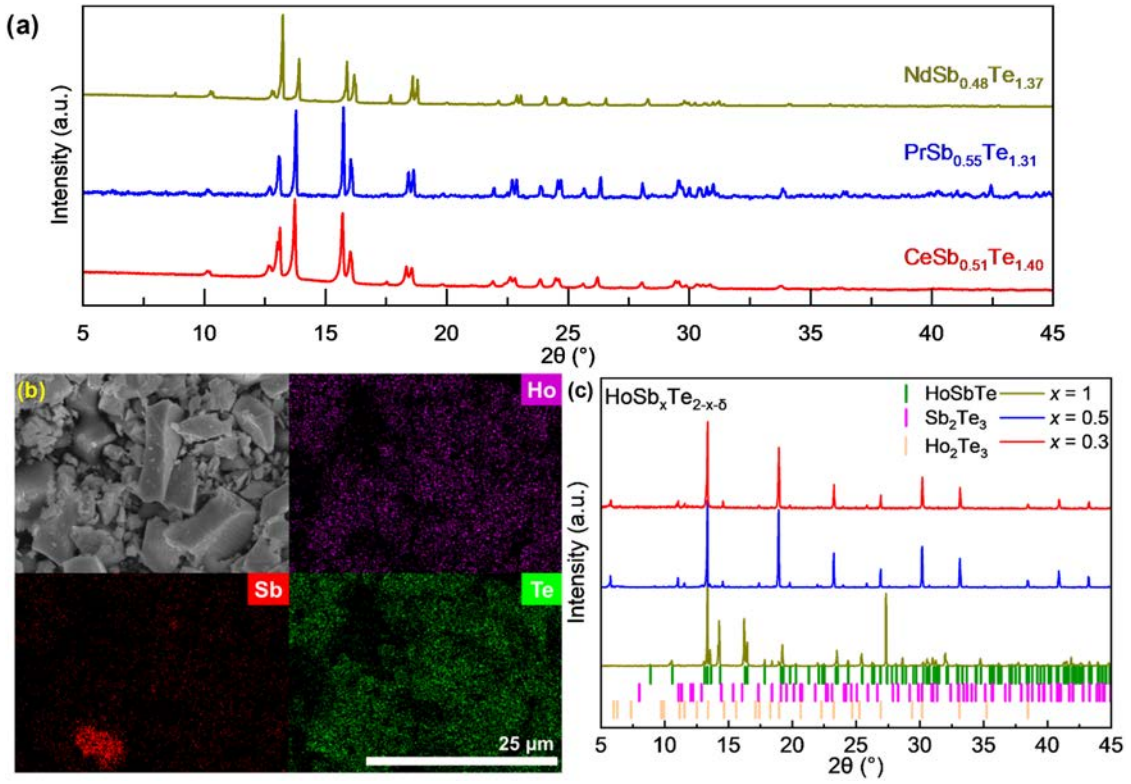

Figure 2. (a) PXRD patterns of successfully synthesized $LnSb_xTe_{2-x-\delta}$ phases. Patterns of prepared samples of $NdSb_{0.48}Te_{1.37}$ and $PrSb_{0.56}Te_{1.31}$ are closely reminiscent of $CeSb_{0.51}Te_{1.40}$, indicating that the average structure for $LnSb_xTe_{2-x-\delta}$ is approximately isostructural across similar x. (b) SEM image and EDS mapping of a failed attempt to synthesize nonstoichiometric $HoSb_xTe_{2-x-\delta}$. Maps show phase segregation of products into Ho_2Te_3 and Sb_2Te_3. (c) PXRD patterns of $HoSb_xTe_{2-x-\delta}$ synthesis products with varying x. The synthesis of HoSbTe is successful for target composition x = 1, whereas Ho_2Te_3 and Sb_2Te_3 are found to be the sole products for x = 0.3, 0.5.

present our efforts to stabilize small Ln by alleviating lattice strain with the addition of La to $HoSb_xTe_{2-x-\delta}$, also introducing an additional parameter to tune the magnetic properties.

EXPERIMENTAL SECTION

Synthesis of $LnSb_xTe_{2-x-\delta}$ Phases. Powders and single crystals of $LnSb_xTe_{2-x-\delta}$ were synthesized by using a chemical vapor transport (CVT) method. All samples were prepared from Ln pieces (Sources/Purities here), Sb shot (Alfa Aesar, 99.999%), and Te pieces, which were purified in-house after purchase from a commercial source (Sigma-Aldrich, 99.999%). For some samples, powder precursors were synthesized prior to CVT growth. Elements were loaded in the desired stoichiometry into a 12 mm fused quartz tube and sealed with a flame under vacuum, with an Ar backfill at approximately 60 mTorr, and subsequently heated to 1000 °C over 12 h, held for 2 days, and cooled over 12 h in a box furnace. The resulting powders were ground and loaded into a 15 mm tube with 120 mg of I_2 as a vapor transport agent, sealed under vacuum resulting in tubes of 6−8 cm in length. CVT growth was then carried out by placing the tubes in a single zone tube furnace, with the powder-containing end of the tube placed in the center of the furnace to create a thermal gradient at the sink side. The tubes were heated to 1000 °C over 12 h, held for 7 days, and cooled over 12 h, resulting in crystals or powder formed at the sink end. In many successful cases, powder of the desired phase was also observed at the source end of the tube after growth.

Sample Characterization. Powder X-ray diffraction (PXRD) data were collected on an STOE STADI P PXRD instrument with a Mo-K_α radiation source, working in Debye−Scherrer geometry. Selected single crystals or powder samples were ground and loaded into 0.3 mm capillaries (Hilgenberg, glass no. 140) inside an Ar-filled glovebox. For successfully synthesized $LnSb_xTe_{2-x-\delta}$ samples, the space group and unit cell were confirmed via Le Bail refinement using GSAS-II or TOPAS. Peak asymmetry is widely observed due to the instrument geometry and is modeled as such in Le Bail refinement. Phase analysis of unsuccessful reactions was performed using the Search/Match module within the STOE WinXPow software package. Reference PXRD patterns of known phases were retrieved from the ICDD PDF database.

Scanning electron microscopy (SEM) images and energy-dispersive spectroscopy (EDS) spectra were collected with a Verios 460 extreme high-resolution scanning electron microscope and a Quanta 200 FEG environmental-SEM, each equipped with an Oxford energy-dispersive X-ray spectrometer.

Single-Crystal X-ray Diffraction. Single-crystal X-ray diffraction (SCXRD) data for $NdSb_{0.30}Te_{1.61}$ and $NdSb_{0.23}Te_{1.70}$ were collected on a Bruker D8 VENTURE with a PHOTON 3 CPAD detector and a Rigaku XtaLAB Synergy with a HyPix 6000 detector, respectively, using a monochromated MoK_α radiation source. Integrated data were corrected with either a multiscan absorption correction using SADABS or a numerical absorption correction using CrysAlisPro. Both samples exhibited satellite reflections indicative of structural modulation. $NdSb_{0.23}Te_{1.70}$ could be indexed commensurately as a 3-fold supercell, indicative of a CDW with propagation wavevector $\boldsymbol{q}$ = 1/3$\boldsymbol{b}$*. $NdSb_{0.23}Te_{1.70}$ was solved via SHELXT[51] using intrinsic phasing and refined with SHELXL[52] using the least-square method, as implemented in the OLEX2 program.[53] $NdSb_{0.30}Te_{1.61}$ could be indexed with an incommensurate propagation wavevector $\boldsymbol{q}$ = 0.2855$\boldsymbol{b}$*. Thus, refinement was carried out using the superspace approach, where the displacive modulation of atomic positions is expressed by a periodic function, represented by a 3 + 1-dimensional superspace group. Solution and refinement were carried out using the program JANA2020.[54] The refinement model implemented parameters for positional, ADP, and site occupancy modulations. At laboratory-accessible X-ray wavelengths, Sb and Te cannot be

https://doi.org/10.1021/acs.chemmater.4c02198
Chem. Mater. XXXX, XXX, XXX−XXX

distinguished from one another on the same crystallographic site due to their closeness in atomic number (Z_{Sb} = 51, Z_{Te} = 52). Thus, atomic occupancy within the Sb/Te square net was constrained to the stoichiometry derived from EDS for all refinements.

RESULTS AND DISCUSSION

New $LnSb_xTe_{2-x-\delta}$ and Synthetic Limitations. While end members of $LnSb_xTe_{2-x-\delta}$ with x = 1 and 0 have been reported,[21,24−27,29−36,43−48] the synthesis of many phases with intermediate x do not yet exist in the literature. Synthesis attempts were limited to CVT methods due to the well-documented potential to access formation and crystal growth of nonstoichiometric phases. While some 1:1:1 end members have been successfully made using Sb or Te flux, they have limited utility in accessing the full composition space due to the large excess of either element required. Eutectic salt fluxes of LiCl/RbCl have been successfully employed to grow crystals of $LaSb_xTe_{2-x-\delta}$ in the work of Dimasi et al., the first paper that reported and characterized phases with intermediate x. The salt flux method has been extended to other lanthanide-containing square net compounds but has not been further explored in $LnSb_xTe_{2-x-\delta}$. While outside the scope of this work, it cannot be ruled out that such alternative routes may yield successful results. We report the successful synthesis of several of these phases across Ln = Pr, Nd, and Tb. No attempts were made to synthesize $EuSb_xTe_{2-x-\delta}$ compounds, due to the tendency for Eu to remain in a + 2 oxidation state, incompatible with the required charge balancing to stabilize $LnSb_xTe_{2-x-\delta}$.

For all successful syntheses, PXRD data is consistent with space group symmetry for previously studied $LnSb_xTe_{2-x-\delta}$.[37,39,40,43,50] PXRD data of the Nd series is consistent with the recent reports by Hu et al.;[50] previously unreported Pr and Tb patterns resemble the reflection positions and evolving peak splitting of other $LnSb_xTe_{2-x-\delta}$, with variation consistent with the size of their respective Ln^{3+} species at similar x (Figure 2a, Supporting Figures 1−3). The elemental composition of the successfully synthesized compounds has been confirmed via EDS (Supporting Figures 4−17) Single-crystal X-ray diffraction was carried out on two previously unreported Nd phases, $NdSb_{0.30}Te_{1.61}$ and $NdSb_{0.23}Te_{1.70}$, with their solved crystal structures presented in Supporting Figures 9 and 10. Both compounds were found to exhibit single-**q** CDW modulation along the crystallographic b axis, consistent with other $LnSb_xTe_{2-x-\delta}$ at similar x, further corroborating that the presence of evolving CDW is consistent across different Ln. Bonding interactions are depicted for distances equal to or shorter than atomic distances observed in the undistorted, near-stoichiometric phase $NdSb_{0.91}Te_{0.89}$ we have previously reported,[43] serving as a reference to compare square-net distortions and interlayer distances.

$NdSb_{0.23}Te_{1.70}$ was commensurately indexed and solved as a 3-fold superstructure in space group *Pmmn*. The crystal structure bears a significant resemblance to the 3-fold CDW Ce analogue $CeSb_{0.34}Te_{1.66}$, in which the square net has distorted into chains of fused four-membered rings, sandwiched by NdTe layers.[40] The (Sb/Te)-(Sb/Te) bond length within the rings is 3.0083(6) Å, while the distance between the atoms in adjacent rings is 3.3462(13) Å. Within the NdTe layer, modulation is small for Nd−Te bonds, where the bond distances nearly parallel to the ab plane range 3.2296(5) to 3.2458(4) Å, with more pronounced modulation along c, with distances ranging 3.2128(11) to 3.2651(9) Å. Most interestingly, the structure exhibits a significant interaction between the distorted square net and the NdTe layer, where the shortest Nd-(Sb/Te) contact is found to be 3.2572(10) Å.

$NdSb_{0.30}Te_{1.61}$ was found to exhibit an incommensurate CDW with a propagation wavevector $\boldsymbol{q}$ = 0.2855$\boldsymbol{b}$*, corresponding to a modulation period of 3.5 unit cells, with the (3 + 1)D superspace group $Pmmn(0\beta0)00s$. Thus, it can be represented with a 7-fold approximant to extract meaningful structure information. The distorted square net contains structural motifs of both adjacent 3-fold and 4-fold family members, exhibiting a pattern of zigzag chains (intrachain bond range: 2.89977(12) to 2.97416(12) Å), isolated atoms (chain-atom distance range: 3.05946(11) to 3.30224(11) Å), and fused four-membered rings (intraring bond: 2.97598(11) to 3.05711(11) Å, chain-ring distance 3.30336(11) to 3.32533(11) Å). Bond distances within the NdTe layer are slightly larger in comparison with $NdSb_{0.23}Te_{1.70}$, with distances along ab ranging 3.21889(11) to 3.23863(11) Å, and along c ranging 3.2332(3) to 3.2810(3) Å. Interactions between the Nd−Te layer and the distorted net are once again observed, with Nd-(Sb/Te) bond distances as short as 3.26601(14) Å, albeit with a lower frequency in comparison to that of $NdSb_{0.23}Te_{1.70}$. The observation of interlayer bonding in these phases is a notable departure from most previously reported CDW phases, where interlayer Ln-Te distances uniformly exceed intralayer Ln-(Sb/Te) distances, with the sole exception of 4-fold CDW compound $GdSb_{0.21}Te_{1.69}$.[39] This result will become relevant in our analysis of stability trends in the following section.

Attempts to synthesize nonstoichiometric members containing Ln smaller than Tb, ranging from Dy to Lu, were unsuccessful and characterized by EDS and XRD (Supporting Figures 18−27, Supporting Tables 8−11). Attempts to synthesize $HoSb_xTe_{2-x-\delta}$ (Figure 2b,c) are representative of other unsuccessful syntheses. While attempts to reproduce the synthesis of known LnSbTe were successful, attempts to decrease x would result in the formation of binaries Ln_2Te_3, $LnTe_3$, Sb_2Te_3, LnI_3, and alloyed pieces of elemental Sb and Te. Some unique exceptions are found in attempts to synthesize $ErSb_xTe_{2-x-\delta}$, where reaction with transport agent I_2 yields a metallic $Er_{17.3}Te_{24}I_8$[55] (Supporting Figures 21 and 22, Table 9), and $YbSb_xTe_{2-x-\delta}$, where the preferred 2^+ oxidation state leads to the formation of unrelated $YbSb_2Te_4$[56] (Supporting Figure 25). While similar reaction conditions across Ln = La−Tb result in the desired phases, the consistent failure to form them in Ho and beyond suggests a structural stability limit as Ln becomes smaller. The origins of this stability limit are discussed in the following section.

Stability Phase Diagram of $LnSb_xTe_{2-x-\delta}$. Figure 3 presents the compiled results of the synthesis attempts presented in this work and the reported literature. As mentioned previously, the formation of $LnSb_xTe_{2-x-\delta}$ with intermediate x appears to be unstable for Ln smaller than Tb. Notably, x = 1 and x = 0 phases can be synthesized for Dy, whereas only HoSbTe was formed via CVT.

Hints to the origin of the instability of late Ln phases exist in reported failures to synthesize $HoTe_2$ and $ErTe_2$ by Wang and Steinfink.[22] They suggest that with decreasing Ln size, the distance between the LnTe layers and the square net compresses, as well as the bond length in LnTe layers themselves. This strain compresses the Te−Te bond length within the square net, leading to destabilization under atmospheric conditions. This is further corroborated by reports

https://doi.org/10.1021/acs.chemmater.4c02198
Chem. Mater. XXXX, XXX, XXX−XXX

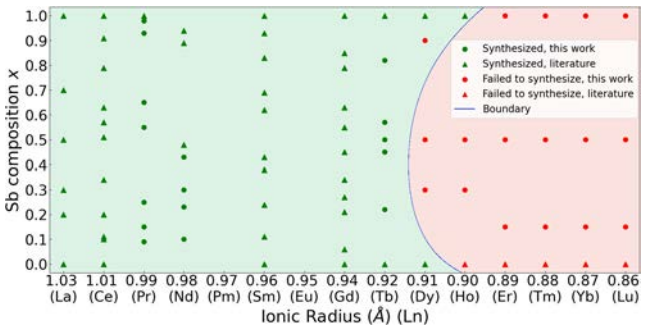

Figure 3. Stability phase diagram of $LnSb_xTe_{2-x-\delta}$ across Ln and $0 \leq x \leq 1$, compiled from our synthesis efforts and the reported literature attempted without high-temperature, high-pressure methods.[21−40,43] A stability boundary is observed for late Ln as the size of Ln decreases.

of successful high-pressure, high-temperature syntheses of $LnTe_{2-\delta}$ for Ln = Ho, Er, Tm, and Lu.[57] These compounds are isostructural with the average structures of $LnTe_{2-\delta}$ phases that are stable at standard pressure. While they can be subsequently isolated at standard pressure and temperature, they are unstable, decomposing on the order of several days. Given that Sb and Te are nearly isosteric, we posit that this trend can be extended to $LnSb_xTe_{2-x-\delta}$.

For known stoichiometric LnSbTe phases (Ln = La−Ho, excluding *Pm* and Eu), the in-plane lattice parameter *a* is directly governed by the Sb−Sb distance (d_{Sb-Sb}), which ranges from 2.980 to 3.111 Å. We can presume that the hypervalent bonding of the square net is stable within this range. While our attempts to synthesize ErSbTe and TmSbTe failed, Plokhih et al. report success in polycrystalline samples using excess Sb, albeit with impurities present.[45] While nonstoichiometric phases can relieve this strain by CDW formation, the loss of polyanionic character in the Sb^- net breaks the charge balance in LnSbTe. Conversely, CDW and vacancy partially restore the charge balance in $LnSb_xTe_{2-x-\delta}$ and $LnTe_{2-\delta}$. As *x* increases in $LnSb_xTe_{2-x-\delta}$, the square net distorts into smaller subunits of localized Sb-(Sb/Te), where (d_{Sb-Sb}) ranges from 2.959 Å in $NdSb_{0.48}Te_{1.37}$ to 2.816 Å in $GdSb_{0.21}Te_{1.69}$, indicating that the CDW stabilizes the net.[39,43] However, this stabilization is localized to the distorted square net, as the Ln−Te bond length remains nearly constant for all of *x*.

The presence of related square net compounds $LnTe_3$ in failed reactions provides further insight. A limited number have been grown by CVT, while their synthesis via self-flux or Te flux occurs at lower temperatures than our CVT attempts. $LnTe_3$ is stable for Ln = La−Tm and is structurally similar to $LnSb_xTe_{2-x-\delta}$, composed of $LnTe_2$ layers separated by an additional Te square net layer. Its stability can be attributed to the additional square net, which relieves the interlayer strain present in the $LnSb_xTe_{2-x-\delta}$ family.[22] The in-plane lattice parameter *a* is nearly identical to its counterparts in $LnSb_xTe_{2-x-\delta}$, as are the Ln−Te bond lengths, further indicating that primarily interlayer strain limits the latter's stability.

The presence of interlayer bonding discovered in $NdSb_{0.30}Te_{1.61}$ and $NdSb_{0.23}Te_{1.70}$ gives further insight into the stability limit of single-**q** CDW phases with respect to Ln. Interlayer bonding increases with *x*, and it is likely exacerbated by decreasing Ln size. With the evolving CDW distortion, the square net splits into smaller discrete anionic subunits, which offer multiple unique coordination environments for neighboring Ln. As Ln size decreases, it is likely that Coulombic attraction between Ln and the broken net increases, suggested by shrinking Gd-(Sb/Te) distances in $GdSb_{0.21}Te_{1.69}$ compared to the Nd phases. This stability trend is reminiscent of the previously discussed hypothesis by Wang et al., providing a potential explanation for why end members for Dy and Ho phases are stable, whereas intermediate *x* compounds do not form, as shrinking Ln drives both interlayer and intralayer lattice strain. Given that $CeSb_xTe_{2-x-\delta}$ exhibits a phase transition from a single-**q** CDW, localized to the square net, to a three-dimensional multi-**q** CDW phase, this also suggests that interlayer interactions inform the critical point in the evolving CDW phase diagram.

Stabilization of Late Ln into $LnSb_xTe_{2-x-\delta}$ via La Substitution. Given that the stability limit of $LnSb_xTe_{2-x-\delta}$ is governed by the size of Ln, late Ln may be stabilized by substitution into phases containing larger Ln to accommodate the lattice strain. We substituted Ho into $LaSb_xTe_{2-x-\delta}$ as a proof of concept, successfully yielding $La_{1-y}Ho_ySb_xTe_{2-x-\delta}$

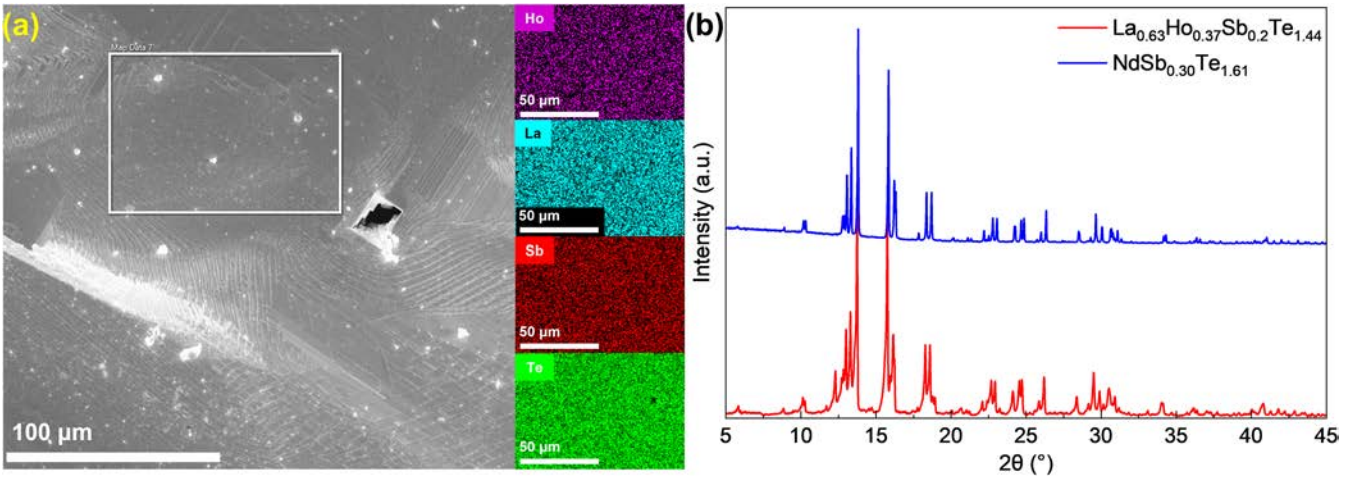

Figure 4. (a) SEM image and EDS mapping of a crystal of $La_{0.63}Ho_{0.37}Sb_{0.2}Te_{1.44}$. Elemental maps indicate sample homogeneity, confirming the successful substitution of ho into the $LaSb_xTe_{2-x-\delta}$ lattice. (b) PXRD patterns of $La_{0.63}Ho_{0.37}Sb_{0.2}Te_{1.44}$. Comparison to a compound with similar *x*, $NdSb_{0.3}Te_{1.61}$, suggests that its average structure is isostructural to other $LnSb_xTe_{2-x-\delta}$.

https://doi.org/10.1021/acs.chemmater.4c02198
Chem. Mater. XXXX, XXX, XXX−XXX

phases. Targeting presumed CDW phases, reactions were carried out with varying La substitution ($0 \leq y \leq 1$), while Sb composition was held constant at $x = 0.5$. At low Ho loadings ($y \leq 0.1$), EDS mapping of reaction products indicates the formation of $LaSb_xTe_{2-x-\delta}$ with no detectable Ho incorporation (Supporting Figure 28). Ho silicates were observed on the surfaces of the samples, suggesting the reaction of Ho with the quartz reaction tube. As y is increased, stable phases with homogeneous incorporation of both Ln are achieved and confirmed by EDS (Figure 4a, Supporting Figures 29 and 30). In all successful samples, x is significantly lower than the targeted composition ($x \approx 0.25$), consistent with the results of other $LnSb_xTe_{2-x-\delta}$ syntheses. PXRD of $La_{0.63}Ho_{0.37}Sb_{0.2}Te_{1.44}$ (Figure 4b) indicates that the dominant phase is structurally similar to $LnSb_xTe_{2-x-\delta}$ of a similar x. As targeted y is increased, a solubility limit is observed at $y \approx 0.38$, as excess Ho reacts with quartz or forms side products identified in unsuccessful $HoSb_xTe_{2-x-\delta}$ synthesis. This limits the formation of the desired $(La/Ho)Sb_xTe_{2-x-\delta}$ phase, requiring careful selection of single crystals from the reaction mixture for XRD analysis. PXRD of a sample with target composition $y = 0.8$ (EDS composition $La_{0.62}Ho_{0.38}Sb_{0.13}Te_{1.72}$) bears a resemblance to that of $La_{0.63}Ho_{0.37}Sb_{0.2}Te_{1.44}$ (Supporting Figure 31).

Le Bail refinement of $La_{0.63}Ho_{0.37}Sb_{0.2}Te_{1.44}$ (Supporting Figure 32) yields a unit cell with space group *Pmmn* and lattice parameters $a = 4.39$ Å, $b = 4.46$ Å, and $c = 9.18$ Å. However, several significantly weaker reflections are missing from the fit, reducing the overall quality of the refinement. While possibly an impurity phase, these outstanding reflections are likely indicative of a superstructure derived from a CDW, or from possible La/Ho ordering which could optimize lattice strain. This possibility is also supported by our SCXRD findings, as smaller Ln are more likely to interact strongly with the distorted square net, which could lead to site preference or the emergence of a multi-**q** CDW phase. Despite this, the results confirm that orthorhombic $La_{0.63}Ho_{0.37}Sb_{0.2}Te_{1.44}$ can be synthesized. Assuming statistical mixing of La and Ho on the Ln^{3+} site, the effective atomic radius can be calculated as the stoichiometrically weighted average of the six-coordinate Shannon radii $r_{Ln} = 0.63r_{La^{3+}} + 0.37r_{Ho^{3+}} = 1.12$ Å, approximate to r_{Nd3+}. This is corroborated by the consistency of the determined lattice parameters with those in the range reported for orthorhombic $NdSb_xTe_{2-x-\delta}$. It is unclear if size effects limit the stability of mixed La/Ho products, as smaller cell volumes can be observed in $SmSb_xTe_{2-x-\delta}$ and $GdSb_xTe_{2-x-\delta}$.[37,39] This invites future study of $La_{1-y}Ho_ySb_xTe_{2-x-\delta}$ and phases with smaller Ln substituted, to explore the possibility of superstructure ordering and its influence on Ln solubility. We speculate that in the absence of additional order, the solubility limit will continue to decrease with the Ln radius, as the stability boundary would likely be reached at even lower substitution levels.

The successful synthesis and crystal growth of $La_{1-y}Ho_ySb_xTe_{2-x-\delta}$ shows promise to expand the accessible composition space of $LnSb_xTe_{2-x-\delta}$, by introducing Ln as an additional tunable parameter and suggesting that stabilizing even smaller Ln in the lattice may be feasible.

CONCLUSIONS

In conclusion, we investigated the stability and synthetic feasibility of the entire composition space for $LnSb_xTe_{2-x-\delta}$, generating a stability phase diagram of Ln vs x. We report the synthesis of heretofore undiscovered phases within $PrSb_xTe_{2-x-\delta}$ and $TbSb_xTe_{2-x-\delta}$, confirmed by EDS and PXRD. While $x = 1$ and $x = 0$ phases are stable to Ho and Dy respectively, a stability limit is found at Tb for intermediate x. Analysis of failed reaction products by XRD and EDS suggests that the stability boundary is governed by the size of Ln, where the interlayer lattice strain increases as Ln becomes smaller, leading to the formation of other stable binary phases. We find that Ln beyond the phase boundary can be stabilized by substitution into larger $LnSb_xTe_{2-x-\delta}$ to accommodate the increased strain. This method affords significant substitution, demonstrated by the synthesis of $La_{1-y}Ho_ySb_xTe_{2-x-\delta}$ with y values of up to 0.38, confirmed by XRD and EDS. The potential to extend this method to smaller Ln expands the range of possible phases in the $LnSb_xTe_{2-x-\delta}$ system, offering new tunable parameters to study the interplay of dilute and mixed magnetism with topological states.

ASSOCIATED CONTENT

Supporting Information

The Supporting Information is available free of charge at https://pubs.acs.org/doi/10.1021/acs.chemmater.4c02198.

Scanning electron microscopy images; energy-dispersive spectroscopy; powder X-ray diffraction data; and single-crystal X-ray diffraction crystal structure data (PDF)

NdSb0p3Te1p61 (CIF)

NdSb0p23Te1p7 (CIF)

AUTHOR INFORMATION

Corresponding Author

Leslie M. Schoop − *Department of Chemistry, Princeton University, Princeton, New Jersey 08544, United States;* orcid.org/0000-0003-3459-4241; Email: lschoop@princeton.edu

Authors

Tyger H. Salters − *Department of Chemistry, Princeton University, Princeton, New Jersey 08544, United States*

James Colagiuri − *Department of Chemistry, Princeton University, Princeton, New Jersey 08544, United States*

Andre Koch Liston − *Department of Chemistry, Princeton University, Princeton, New Jersey 08544, United States*

Josh Leeman − *Department of Chemistry, Princeton University, Princeton, New Jersey 08544, United States*

Tanya Berry − *Department of Chemistry, Princeton University, Princeton, New Jersey 08544, United States;* orcid.org/0000-0002-1583-2120

Complete contact information is available at: https://pubs.acs.org/10.1021/acs.chemmater.4c02198

Notes

The authors declare no competing financial interest.

ACKNOWLEDGMENTS

This work was supported by an NSF CAREER grant (DMR-2144295) to L.M.S. Additional support was provided by the Air Force Office of Scientific Research under award number FA9550-20-1-0246. This work was further supported by the Gordon and Betty Moore Foundation (EPiQS Synthesis Award) through grant GBMF9064, and the David and Lucile Packard Foundation. T.B. acknowledges support from NSF-MRSEC through the Princeton Center for Complex Materials

NSF-DMR-2011750. T.H.S. is grateful to Marceline Martineau for helpful discussion.

REFERENCES

(1) Klemenz, S.; Lei, S.; Schoop, L. M. Topological semimetals in square-net materials. *Annu. Rev. Mater. Res.* **2019**, *49*, 185−206.

(2) Klemenz, S.; Hay, A. K.; Teicher, S. M.; Topp, A.; Cano, J.; Schoop, L. M. The role of delocalized chemical bonding in square-net-based topological semimetals. *J. Am. Chem. Soc.* **2020**, *142*, 6350−6359.

(3) Klemenz, S.; Schoop, L.; Cano, J. Systematic study of stacked square nets: From Dirac fermions to material realizations. *Phys. Rev. B* **2020**, *101*, No. 165121.

(4) Schoop, L. M.; Pielnhofer, F.; Lotsch, B. V. Chemical principles of topological semimetals. *Chem. Mater.* **2018**, *30*, 3155−3176.

(5) Liu, J.; Hu, J.; Cao, H.; Zhu, Y.; Chuang, A.; Graf, D.; Adams, D. J.; Radmanesh, S. M. A.; Spinu, L.; Chiorescu, I.; Mao, Z. Nearly massless Dirac fermions hosted by Sb square net in $BaMnSb_2$. *Sci. Rep.* **2016**, *6*, No. 30525.

(6) Park, J.; Lee, G.; Wolff-Fabris, F.; Koh, Y. Y.; Eom, M. J.; Kim, Y. K.; Farhan, M. A.; Jo, Y. J.; Kim, C.; Shim, J. H.; Kim, J. S. Anisotropic Dirac Fermions in a Bi Square Net of $SrMnBi_2$. *Phys. Rev. Lett.* **2011**, *107*, No. 126402.

(7) Hu, J.; Tang, Z.; Liu, J.; Liu, X.; Zhu, Y.; Graf, D.; Myhro, K.; Tran, S.; Lau, C. N.; Wei, J.; Mao, Z. Evidence of Topological Nodal-Line Fermions in ZrSiSe and ZrSiTe. *Phys. Rev. Lett.* **2016**, *117*, No. 016602.

(8) Wu, H.; Hallas, A. M.; Cai, X.; et al. Nonsymmorphic symmetry-protected band crossings in a square-net metal PtPb4. *npj Quantum Mater.* **2022**, *7*, 1−7.

(9) Wang, K.; Graf, D.; Wang, L.; Lei, H.; Tozer, S. W.; Petrovic, C. Two-dimensional Dirac fermions and quantum magnetoresistance in $CaMnBi_2$. *Phys. Rev. B* **2012**, *85*, No. 041101.

(10) Borisenko, S.; Evtushinsky, D.; Gibson, Q.; Yaresko, A.; Koepernik, K.; Kim, T.; Ali, M.; van den Brink, J.; Hoesch, M.; Fedorov, A.; Haubold, E.; Kushnirenko, Y.; Soldatov, I.; Schäfer, R.; Cava, R. J. Time-reversal symmetry breaking type-II Weyl state in $YbMnBi_2$. *Nat. Commun.* **2019**, *10*, No. 3424.

(11) Schoop, L. M.; Ali, M. N.; Straßer, C.; Topp, A.; Varykhalov, A.; Marchenko, D.; Duppel, V.; Parkin, S. S. P.; Lotsch, B. V.; Ast, C. R. Dirac cone protected by non-symmorphic symmetry and three-dimensional Dirac line node in ZrSiS. *Nat. Commun.* **2016**, *7*, 1−7.

(12) Gebauer, P.; Poddig, H.; Corredor-Bohorquez, L. T.; Menshchikova, T. V.; Rusinov, I. P.; Golub, P.; Caglieris, F.; Benndorf, C.; Lindemann, T.; Chulkov, E. V.; Wolter, A. U. B.; Büchner, B.; Doert, T.; Isaeva, A. Heavy-Atom Antiferromagnet GdBiTe: An Interplay of Magnetism and Topology in a Symmetry-Protected Topological Semimetal. *Chem. Mater.* **2021**, *33*, 2420−2435.

(13) Papoian, G. A.; Hoffmann, R. Hypervalent Bonding in One, Two, and Three Dimensions: Extending the Zintl−Klemm Concept to Nonclassical Electron-Rich Networks. *Angew. Chem., Int. Ed.* **2000**, *39*, 2408−2448.

(14) Papoian, G. A.; Hoffmann, R. Hypervalent Bonding in One, Two, and Three Dimensions: Extending the Zintl−Klemm Concept to Nonclassical Electron-Rich Networks. *Angew. Chem., Int. Ed.* **2000**, *39*, 2408−2448.

(15) Grüner, G. *Density waves in solids*, Volume 89 of Frontiers in Physics; Advanced Book Program; Addison-Wesley Pub. Co. Reading, 1994.

(16) Zunger, A. Beware of plausible predictions of fantasy materials. *Nature* **2019**, *566*, 447−449.

(17) Bradlyn, B.; Elcoro, L.; Cano, J.; Vergniory, M. G.; Wang, Z.; Felser, C.; Aroyo, M. I.; Bernevig, B. A. Topological quantum chemistry. *Nature* **2017**, *547*, 298−305.

(18) Weiland, A.; Chaparro, D. G.; Vergniory, M. G.; Derunova, E.; Yoon, J.; Oswald, I. W. H.; McCandless, G. T.; Ali, M.; Chan, J. Y. Band structure engineering of chemically tunable LnSbTe (Ln = La, Ce, Pr). *APL Mater.* **2019**, *7*, No. 101113.

(19) Vergniory, M. G.; Elcoro, L.; Felser, C.; Regnault, N.; Bernevig, B. A.; Wang, Z. A complete catalogue of high-quality topological materials. *Nature* **2019**, *566*, 480−485.

(20) Wang, Y. C.; Poduska, K. M.; Hoffmann, R.; DiSalvo, F. J. Structure and physical properties of CeSbTe. *J. Alloys Compd.* **2001**, *314*, 132−139.

(21) Park, S. M.; Park, S. J.; Kim, S. J. The Superstructure of Semiconducting $SmTe_{2-x}$. *J. Solid State Chem.* **1998**, *140*, 300−306.

(22) Wang, R.; Steinfink, H. The crystal chemistry of selected AB2 rare earth compounds with selenium, tellurium, and antimony. *Inorg. Chem.* **1967**, *6*, 1685−1692.

(23) Wang, Y.; Qian, Y.; Yang, M.; et al. Spectroscopic evidence for the realization of a genuine topological nodal-line semimetal in LaSbTe. *Phys. Rev. B* **2021**, *103*, No. 125131.

(24) Schoop, L. M.; Topp, A.; Lippmann, J.; et al. Tunable Weyl and Dirac states in the nonsymmorphic compound CeSbTe. *Sci. Adv.* **2018**, *4*, No. eaar2317.

(25) Regmi, S.; Elius, I. B.; Sakhya, A. P.; Sprague, M.; Mondal, M. I.; Valadez, N.; Buturlim, V.; Booth, K.; Romanova, T.; Gofryk, K.; Ptok, A.; Kaczorowski, D.; Neupane, M. Electronic structure in a rare-earth based nodal-line semimetal candidate PrSbTe. *Phys. Rev. Mater.* **2024**, *8*, No. L041201.

(26) Regmi, S.; Smith, R.; Sakhya, A. P.; Sprague, M.; Mondal, M. I.; Elius, I. B.; Valadez, N.; Ptok, A.; Kaczorowski, D.; Neupane, M. Observation of gapless nodal-line states in NdSbTe. *Phys. Rev. Mater.* **2023**, *7*, No. 044202.

(27) Pandey, K.; Mondal, D.; Villanova, J. W.; et al. Magnetic Topological Semimetal Phase with Electronic Correlation Enhancement in SmSbTe. *Adv. Quantum Technol.* **2021**, *4*, No. 2100063.

(28) Venkatesan, B.et al. Direct Visualization of Disorder Driven Electronic Liquid Crystal419 Phases in Dirac Nodal Line Semimetal GdSbTe 2024. http://arxiv.org/abs/2402.18893.

(29) Hosen, M. M.; Dhakal, G.; Dimitri, K.; Maldonado, P.; Aperis, A.; Kabir, F.; Sims, C.; Riseborough, P.; Oppeneer, P. M.; Kaczorowski, D.; Durakiewicz, T.; Neupane, M. Discovery of topological nodal-line fermionic phase in a magnetic material GdSbTe. *Sci. Rep.* **2018**, *8*, No. 13283.

(30) Gao, F.; Huang, J.; Ren, W.; Wu, H.; An, M.; Wu, X.; Zhang, L.; Yang, T.; Wang, A.; Chai, Y.; Zhao, X.; Yang, T.; Li, B.; Zhang, Z. Magnetic and Magnetotransport Properties of the Magnetic Topological Nodal-Line Semimetal TbSbTe. *Adv. Quantum Technol.* **2023**, *6*, No. 2200163.

(31) Elius, I. B.et al. Electronic structure of a nodal line semimetal candidate TbSbTe 2024. http://arxiv.org/abs/2406.09054, last accessed: 19 November 2024.

(32) Stöwe, K. Crystal structure and electronic band structure of $LaTe_2$. *J. Solid State Chem.* **2000**, *149*, 155−166.

(33) Stöwe, K. Crystal structure and magnetic properties of $CeTe_2$. *J. Alloys Compd.* **2000**, *307*, 101−110.

(34) Stöwe, K. Crystal structure, magnetic properties and band gap measurements of $NdTe_{2-x}$ (x = 0.11(1)). *Z. Kristallogr.* **2001**, *216*, 215−224.

(35) Stöwe, K. Die Kristallstruktur von $PrTe_2$. *Z. Anorg. Allg. Chem.* **2000**, *626*, 803−811.

(36) Poddig, H.; Donath, T.; Gebauer, P.; Finzel, K.; Kohout, M.; Wu, Y.; Schmidt, P.; Doert, T. Rare Earth Metal Polytellurides $RETe_{1.8}$ (RE = Gd, Tb, Dy)—Directed Synthesis, Crystal and Electronic Structures, and Bonding Features. *Z. Anorg. Allg. Chem.* **2018**, *644*, 1886−1896.

(37) Pandey, K.; Basnet, R.; Wang, J.; Da, B.; Hu, J. Evolution of electronic and magnetic properties in the topological semimetal $SmSb_xTe_{2-x}$. *Phys. Rev. B* **2022**, *105*, No. 155139.

(38) DiMasi, E.; Foran, B.; Aronson, M.; Lee, S. Stability of charge-density waves under continuous variation of band filling in $LaTe_{2-x}Sb_x$ ($0 \leq x \leq 1$). *Phys. Rev. B* **1996**, *54*, No. 13587.

(39) Lei, S.; Duppel, V.; Lippmann, J. M.; Nuss, J.; Lotsch, B. V.; Schoop, L. M. Charge Density Waves and Magnetism in Topological Semimetal Candidates $GdSb_xTe_{2-x-\delta}$. *Adv. Quantum Technol.* **2019**, *2*, No. 1900045.

https://doi.org/10.1021/acs.chemmater.4c02198
Chem. Mater. XXXX, XXX, XXX−XXX

(40) Singha, R.; Salters, T. H.; Teicher, S. M.; Lei, S.; Khoury, J. F.; Ong, N. P.; Schoop, L. M. Evolving Devil's staircase magnetization from tunable charge density waves in nonsymmorphic Dirac semimetals. *Adv. Mater.* **2021**, *33*, No. 2103476.
(41) Lei, S.; Teicher, S. M. L.; Topp, A.; et al. Band Engineering of Dirac Semimetals Using Charge Density Waves. *Adv. Mater.* **2021**, *33*, No. 2101591.
(42) Singha, R.; Dalgaard, K. J.; Marchenko, D.; Krivenkov, M.; Rienks, E. D. L.; Jovanovic, M.; Teicher, S. M. L.; Hu, J.; Salters, T. H.; Lin, J.; Varykhalov, A.; Ong, N. P.; Schoop, L. M. Colossal magnetoresistance in the multiple wave vector charge density wave regime of an antiferromagnetic Dirac semimetal. *Sci. Adv.* **2023**, *9*, No. eadh0145.
(43) Salters, T. H.; Orlandi, F.; Berry, T.; Khoury, J. F.; Whittaker, E.; Manuel, P.; Schoop, L. M. Charge density wave-templated spin cycloid in topological semimetal $NdSb_xTe_{2-x-\delta}$. *Phys. Rev. Mater.* **2023**, *7*, No. 044203.
(44) Plokhikh, I.; Pomjakushin, V.; Gawryluk, D. J.; Zaharko, O.; Pomjakushina, E. Competing Magnetic Phases in LnSbTe (Ln = Ho and Tb). *Inorg. Chem.* **2022**, *61*, 11399−11409.
(45) Plokhikh, I.; Pomjakushin, V.; Jakub Gawryluk, D.; Zaharko, O.; Pomjakushina, E. On the magnetic structures of 1:1:1 stoichiometric topological phases LnSbTe (Ln = Pr, Nd, Dy and Er). *J. Magn. Magn. Mater.* **2023**, *583*, No. 171009.
(46) Plokhikh, I.; Fabelo, O.; Prodan, L.; Wörle, M.; Pomjakushina, E.; Cervellino, A.; Tsurkan, V.; Kézsmárki, I.; Zaharko, O. Magnetic and crystal structure of the antiferromagnetic skyrmion candidate $GdSb_{0.71}Te_{1.22}$. *J. Alloys Compd.* **2023**, *936*, No. 168348.
(47) Gao, F.; Huang, J.; Ren, W.; Li, M.; Wang, H.; Yang, T.; Li, B.; Zhang, Z. Magnetic and transport properties of the topological compound DySbTe. *Phys. Rev. B* **2022**, *105*, No. 214434.
(48) Yang, M.; Qian, Y.; Yan, D.; Li, Y.; Song, Y.; Wang, Z.; Yi, C.; Feng, H. L.; Weng, H.; Shi, Y. Magnetic and electronic properties of a topological nodal line semimetal candidate: HoSbTe. *Phys. Rev. Mater.* **2020**, *4*, No. 094203.
(49) Lei, S.; Saltzman, A.; Schoop, L. M. Complex magnetic phases enriched by charge density waves in the topological semimetals $GdSb_xTe_{2-x-\delta}$. *Phys. Rev. B* **2021**, *103*, No. 134418.
(50) Chhetri, S. K.; Basnet, R.; Wang, J.; Pandey, K.; Acharya, G.; Nabi, M. R. U.; Upreti, D.; Sakon, J.; Mortazavi, M.; Hu, J. Evolution of magnetism in the magnetic topological semimetal $NdSb_xTe_{2-x-\delta}$. *Phys. Rev. B* **2024**, *109*, No. 184429.
(51) Sheldrick, G. M. SHELXT−Integrated space-group and crystal-structure determination. *Acta Crystallogr., A* **2015**, *71*, 3−8.
(52) Sheldrick, G. M. A short history of SHELX. *Acta Crystallogr., Sect. A:Found. Crystallogr.* **2008**, *64*, 112−122.
(53) Dolomanov, O. V.; Bourhis, L. J.; Gildea, R. J.; Howard, J. a. K.; Puschmann, H. OLEX2: a complete structure solution, refinement and analysis program. *J. Appl. Crystallogr.* **2009**, *42*, 339−341.
(54) Petříček, V.; Henriques, M.; Dušek, V. *JANA2020*—magnetic option. *Acta Crystallogr., Sect. A* **2021**, *77*, C175.
(55) Stöwe, K. Nonstoichiometry in Er−Te Binary and Er−Te−I Ternary Systems. *J. Solid State Chem.* **1998**, *139*, 57−65.
(56) Guloy, A. S.; Gascoin, F.; Chamoire, A.; Tedenac, J. C.; Snyder, G. J. Synthesis and thermoelectric properties of YbSb2Te4. *Phys. Status Solidi RRL* **2007**, *1*, 265−267.
(57) Cannon, J. F.; Hall, H. T. High-pressure, high-temperature syntheses of selected lanthanide-tellurium compounds. *Inorg. Chem.* **1970**, *9*, 1639−1643.

https://doi.org/10.1021/acs.chemmater.4c02198
Chem. Mater. XXXX, XXX, XXX−XXX